Ryanodine Receptor Open Times Are Determined in the Closed State

Michael Fill[1] and Dirk Gillespie[1,*]
[1]Department of Physiology and Biophysics, Rush University Medical Center, Chicago, Illinois

ABSTRACT The ryanodine receptor (RyR) ion channel releases Ca^{2+} from intracellular stores by conducting Ca^{2+} but also by recruiting neighboring RyRs to open, as RyRs are activated by micromolar levels of cytosolic Ca^{2+}. Using long single-RyR recordings of the cardiac isoform (RyR2), we conclude that Ca^{2+} binding to the cytosolic face of RyR while the channel is closed determines the distribution of open times. This mechanism explains previous findings that RyR is not activated by its own fluxed Ca^{2+}. Our measurements also bolster previous findings that luminal $[Ca^{2+}]$ can affect both the cytosolic activation and inactivation sites and that RyR has different gating modes for the same ionic conditions.

In cardiac myocytes, ryanodine receptors (RyRs) release Ca^{2+} from the sarcoplasmic reticulum to initiate muscle contraction. Because RyRs open in response to micromolar $[Ca^{2+}]$, the efflux of Ca^{2+} through one RyR is amplified by the recruitment of nearby RyRs. Although this inter-RyR Ca^{2+}-induced Ca^{2+} release is largely understood, one open question is the extent to which the Ca^{2+} released by a RyR acts on itself (feedthrough activation).

Previous studies showed that RyR generally does not react to its own fluxed Ca^{2+}, with feedthrough activation only for superphysiological currents (>3 pA, compared to ~0.4 pA under physiological conditions) (1,2), or for RyRs that are hypersensitive to Ca^{2+} by the application of caffeine (2) or ATP (3), or in the absence of cytosolic Mg^{2+} (3,4). ATP and Mg^{2+} potently modulate RyR Ca^{2+} sensitivity and are present at high concentrations in cells. Therefore, including these substances is vital when evaluating the physiological role of feedthrough activation. Our experiments with both ATP and Mg^{2+} at physiological cytosolic levels show that RyR does not see its own fluxed Ca^{2+}; the open probability (P_o) (Fig. 1 A) is independent of Ca^{2+} flux <1 pA (Fig. 1 B).

RyR not reacting to its own fluxed Ca^{2+} is difficult to reconcile with other data, namely that RyR open time increases with cytosolic $[Ca^{2+}]$ (1,2,5); mean open time (MOT) is shown in Fig. S5. Open channels are thought to close randomly. In that case, open times are defined while the channel is open. However, to be sensitive to cytosolic

$[Ca^{2+}]$, the cytosolic Ca^{2+} binding sites would have to be accessible to Ca^{2+} during the open state and exposed to the fluxed Ca^{2+}, which can raise Ca^{2+} concentration on the cytosolic face to >15 μM for physiological currents (6) and >50 μM in our experiments (Fig. S9). These
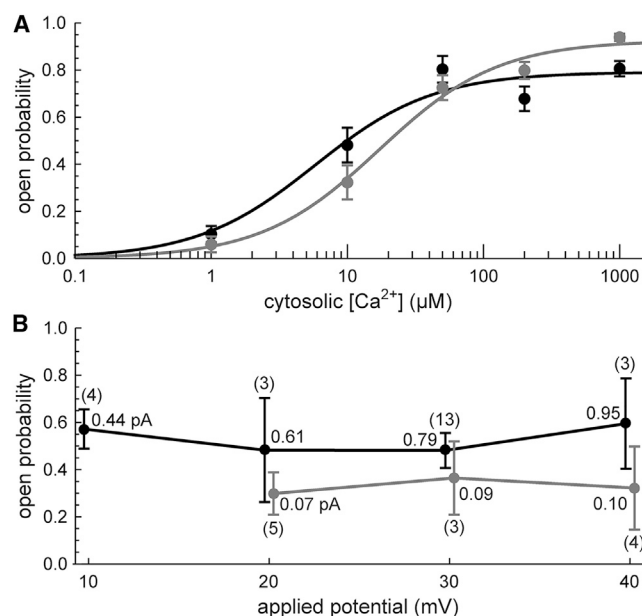

FIGURE 1 (A) P_o versus cytosolic $[Ca^{2+}]$ for high (black) and low (gray) luminal Ca^{2+}. The lines are binding curves. (B) P_o versus applied voltage for high (black) and low (gray) luminal Ca^{2+}. Parentheses: number of recordings. Also listed are calculated Ca^{2+} currents. Cytosolic $[Ca^{2+}]$ is 10 μM. Other $[Ca^{2+}]$ are also independent of potential (data not shown). Details of the P_o analysis, binding curves, and Ca^{2+} currents are in the Supporting Materials and Methods.
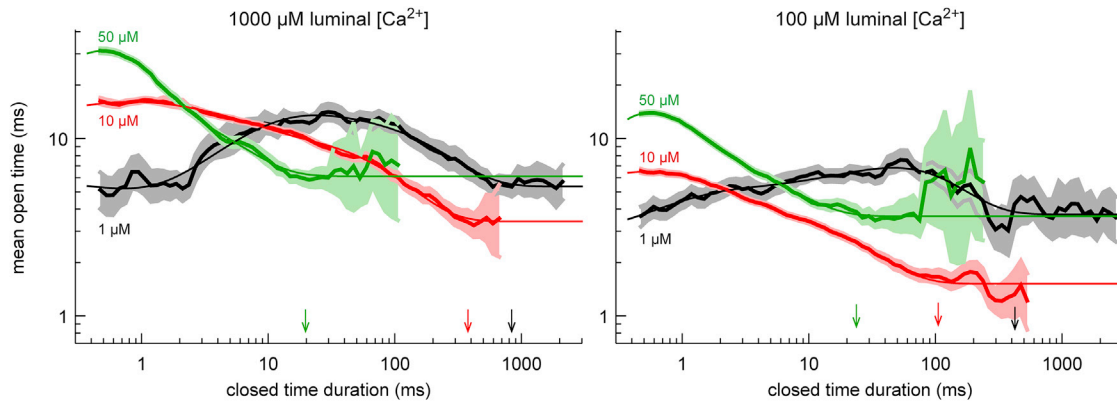
FIGURE 2 MOT versus duration of the previous closed event for 1, 10, and 50 μM cytosolic [Ca^{2+}] and for high (*left*) and low (*right*) luminal [Ca^{2+}]. The thick lines are the mean times of the data, and the shaded areas are the 95% confidence intervals (see Supporting Materials and Methods). The thin lines are fits of a sum of three exponentials, and the arrows indicate when these fits approximately reach steady state (i.e., $4\tau_3$, as defined in Fig. 3). Fig. S10 *A* shows the same for 200 and 1000 μM. Fig. S10 *B* shows mean closed time versus open duration. To see this figure in color, go online.

are substantially larger than needed to activate RyR (Fig. 1 *A*), leading to feedthrough activation.

Here, we test a hypothesis that explains how RyR open times can depend on cytosolic [Ca^{2+}] without having feedthrough activation: RyR open-time distributions are determined in the closed state, before the channel opens.

We do this by analyzing single-RyR2 recordings taken under conditions with high (1000 μM) and low (100 μM) luminal Ca^{2+} and with 1, 10, 50, 200, and 1000 μM cytosolic Ca^{2+}. For each condition, we recorded 8–20 channels for a total time of 13–75 min. (Further details are in the Supporting Materials and Methods; Tables S1 and S2.) This was done to ensure that we understand RyR behavior with cell-like cytosolic Ca^{2+}, Mg^{2+}, and ATP levels, but also because

FIGURE 3 The time constants from the exponential fits in Fig. 2 and Fig. S10 *A* as a function of cytosolic [Ca^{2+}] for both high (*solid lines*) and low (*dashed lines*) luminal [Ca^{2+}]. To see this figure in color, go online.

there is variability between channels under identical conditions and within recordings. This variability is ubiquitous (Figs. S4 and S5), but subgroups of channels have identical open- and closed-time distributions, indicating a small number of gating modes for the same ionic condition (Fig. S6), a property that has been previously reported (7–10). Importantly, however, all our analysis is largely independent of this variability, shown in the figures with 95% confidence intervals (see Supporting Material).

We include data with both high and low luminal Ca^{2+} because each is known to affect the channel differently (11–14). RyR exposed to high luminal Ca^{2+} is more responsive to cytosolic Ca^{2+} (Fig. 1 *A*) and is also subject to inactivation at cytosolic [Ca^{2+}] ≥ 200 μM (Fig. S7), whereas at low luminal Ca^{2+} it is not; the high luminal Ca^{2+} case has a marked drop in MOT between 50 and 200 μM that the low luminal Ca^{2+} case does not (Figs. S5 and S8). We will show that at both high and low luminal Ca^{2+}, the open-time distributions are determined in the closed state.

To start the analysis, we plot MOT versus closed-time duration in Figs. 2 and S10 *A*. This shows how open time correlates to the length of the previous closing. (Fig. S13 shows this in a different way.) The curves are not identical, so it is not merely the length of a closing that determines open time. However, the curves overlap significantly when the closures are longer than ~3 ms, and this overlapping is consistent with our hypothesis that open-time distributions are determined in the closed state. We see from Fig. 2 that for each cytosolic [Ca^{2+}], a final MOT is reached; for long enough closures, each curve becomes a constant. Moreover, the higher the cytosolic [Ca^{2+}], the less time it takes to reach this steady state. Based on this, we hypothesize that there is an underlying Ca^{2+}-dependent process that determines channel open-time distributions (and therefore MOT) and that this process is faster at higher cytosolic [Ca^{2+}].

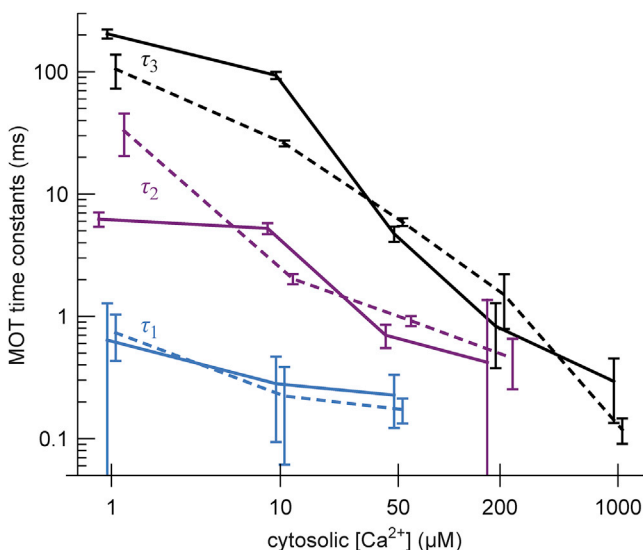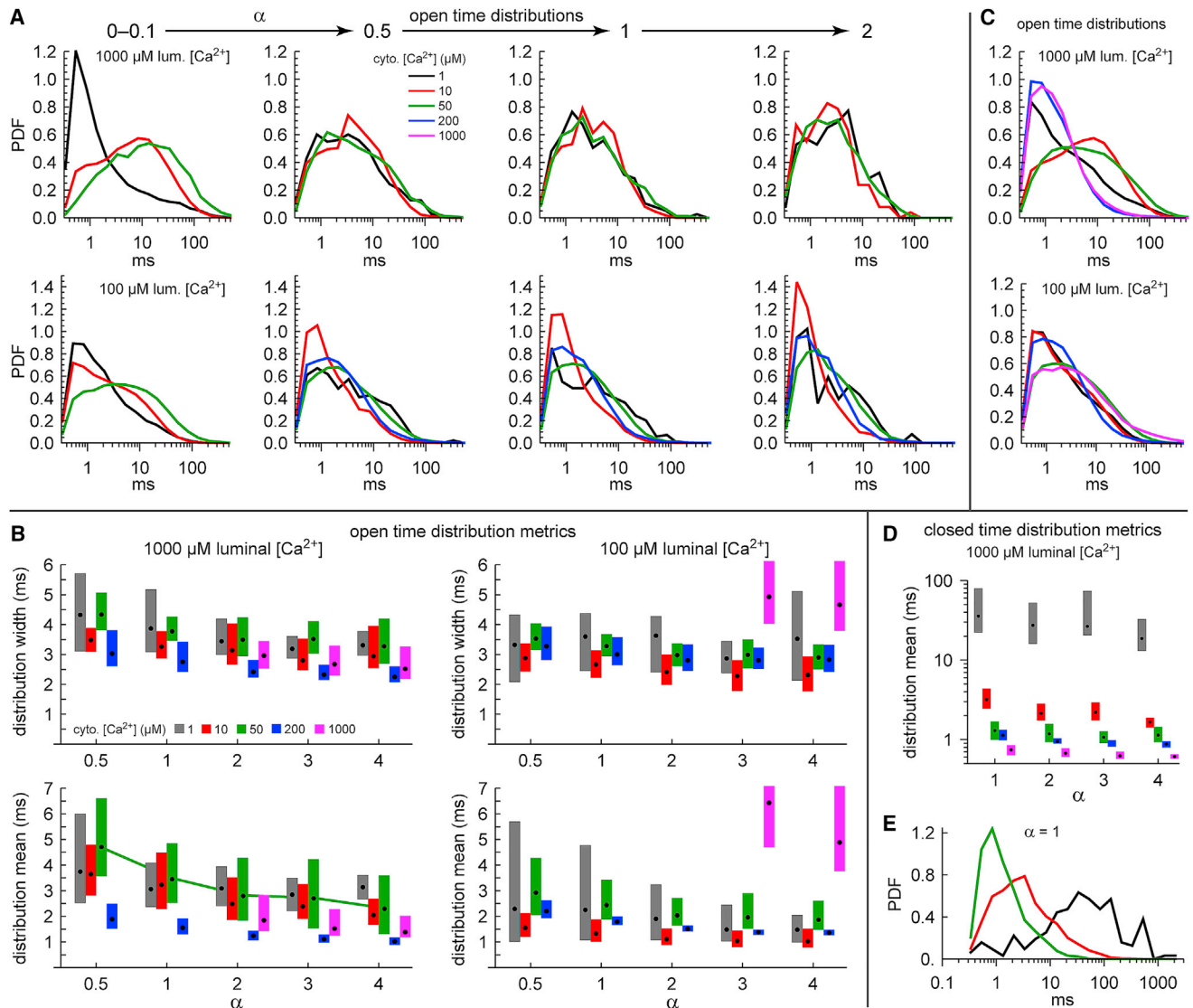FIGURE 4 (*A*) The probability distribution functions (PDFs) of the open times for different scaled times α. When a specific α is listed, all events with closed times t with $0.9\alpha\tau_3 \leq t < 1.1\alpha\tau_3$ are chosen and the distribution of the subsequent open times is shown. Top row, high luminal Ca^{2+}; bottom row, low. (*B*) Metrics of the smoothed histograms described in the **Supporting Materials and Methods**, specifically the standard deviations (*top row*) and means (*bottom row*). (*C*) Open-time PDFs for all recorded openings are shown. (*D*) Distribution means are shown like in (*B*), but for closed-time distributions rather than open-time distributions. (*E*) PDFs are shown as in (*A*), but for closed-time distributions. To see this figure in color, go online.

To identify this underlying process, we fit the curves in Figs. 2 and S10 *A* (*thin lines*) with a sum of up to three exponentials (see Supporting Materials and Methods). Fig. 3 shows the cytosolic $[Ca^{2+}]$ dependence of these time constants.

If the time constants are from a single process, then the largest one (τ_3) defines the timescale it takes to reach steady state. Moreover, if this process defines RyR open-time distributions during the closed state, then the open-time distributions for each cytosolic $[Ca^{2+}]$ should be identical if the closed-time duration t is scaled by the τ_3 for each $[Ca^{2+}]$; i.e., it is not the absolute closed times that determine the open-time distributions, but rather the fraction of time α

through the process ($\alpha = t/\tau_3$ and steady state is reached for $\alpha > \sim4$ (*arrows* in Fig. 2)). We show this in Fig. 4.

Our goal is to show that the open-time distributions are identical for all cytosolic $[Ca^{2+}]$ after a sufficient amount of scaled time (α) has passed. We do this in several ways (with details described below): in Fig. 4 *A*, we show that the distributions look the same; in Fig. 4 *B*, we quantify distribution similarity using two metrics; in Fig. 4, *C–E*, we show negative controls; in Fig. S12, we show that the open-time distributions across cytosolic $[Ca^{2+}]$ are highly correlated.

Fig. 4 *A* shows how the open-time distributions change with α. The top row shows it for high luminal Ca^{2+}, the

bottom for low. Early in the process ($0 < \alpha < 0.1$), the distributions are very different from each other but quickly become the same as α increases. Fig. 4 B shows metrics of the distributions with 95% confidence intervals (see Supporting Materials and Methods); the top row shows the widths of the distributions (standard deviations), the bottom row the means. The purpose of these metrics is to quantify the similarity between the distributions, which are shown in Figs. S1 and S2.

The distributions in Fig. 4 A and the metrics in Fig. 4 B are highly similar, with a few exceptions.

First, at high luminal Ca^{2+}, the distribution means for 200 μM cytosolic Ca^{2+} are below those of the lower concentrations (blue boxes for all α in the lower left panel of Fig. 4 B). This is also true to a lesser extent for 1000 μM cytosolic Ca^{2+} (magenta boxes), whose metrics only appear for $\alpha \geq 2$ because its τ_3 is less than the shortest reliably measurable event time. We suspect that the reason for this is that at these high cytosolic Ca^{2+} concentrations, the Ca^{2+} is binding not only to the activation site of RyR but also to its inactivation site, which decreases MOT (Figs. S5 and S8). If this is the case, then the open-time distributions should be different. However, these distributions are still determined in the closed state, in line with our hypothesis.

Second, at low luminal Ca^{2+}, the distributions for 10 μM cytosolic Ca^{2+} (Fig. 4 A, bottom row, red lines) appear shifted to shorter open times. This is reflected in the distribution means (Fig. 2; red boxes in the lower right panel of Fig. 4 B), but here, the confidence intervals are very close to the distribution means for the other cytosolic $[Ca^{2+}]$; they are all within a fraction of a millisecond of each other. This case is different from the case above (high luminal and 200 μM cytosolic Ca^{2+}) in which the confidence intervals are far from overlapping with other data intervals. Therefore, we believe that this is more a reflection of the variability among channels than a fundamental difference in the distribution shapes. Moreover, if it were significantly different, then this 10 μM cytosolic Ca^{2+} data point would be qualitatively different from surrounding data points at both lower (1 μM) and higher (50 and 200 μM) cytosolic $[Ca^{2+}]$.

Lastly, at low luminal Ca^{2+}, the distribution for 1000 μM cytosolic Ca^{2+} is far different from all other open-time distributions (magenta boxes in the right panels of Fig. 4 B). Both its mean and its width are much larger, which can also be seen in Fig. S10 A (right panel). This is not due to inactivation; mean closed time is shorter than for smaller cytosolic $[Ca^{2+}]$, whereas MOT is longer (Fig. S5). In fact, its P_o is almost 1 (Fig. 1 A). At this point, it is not clear why this data point is so qualitatively different from all the others.

Except for this one outlier and when inactivation is present, we have now shown that open-time distributions of RyR are identical as long as sufficient time has passed in the closed state to be partly through a cytosolic Ca^{2+}-dependent process. This similarity between the open-time distributions is not because the distributions are the same to

begin with; early in the process, the distributions are quite different (Fig. 4 A, first column) and gating may be stochastic (Fig. S13), and the open-time distributions for all the data (i.e., for all opening events) are also very different (Fig. 4 C). Moreover, the similarity is not because the distributions do not change with α; their means change (Fig. 4 B, green line). Lastly, to show a counterexample in which distributions do not cluster, we consider closed- (rather than open-) time distributions and their time constants (Figs. S10 B and S11). Applying the same analysis, we find qualitatively different distributions (Fig. 4, D and E). The point of this is to show that the similarity of the open-time distributions is not expected and to show that closed-time distributions do not seem to be determined during the open state.

Finally, in Fig. S12, we show the Pearson correlation between open-time distributions for all pairs of cytosolic $[Ca^{2+}]$. These high correlations, when combined with the analysis in Fig. 4 B, indicate each pair is the same (except cases noted above). Fig. S12 also shows that $\sim$30% through the process is sufficient to reach identical distributions.

We next focus on the nature of the cytosolic Ca^{2+}-dependent process. Because RyR is activated by cytosolic Ca^{2+}, we hypothesized that this process is Ca^{2+} binding to the activation site on the cytosolic face. A binding process has the necessary characteristics: it is $[Ca^{2+}]$ dependent and requires time to complete, which for simple models occurs through multiple, well-defined time constants. We first tried the simplest model, namely four independent binding sites, one on each of the four identical subunits of RyR. This has one time constant but failed to reproduce the $[Ca^{2+}]$ dependence of the τ_3 (data not shown). Next, we considered a model in which RyR can bind 0–3 Ca^{2+} ions (assuming three Ca^{2+} bound to any of the four subunits is enough to activate the channel) with on and off rates depending on how many are bound. This model describes the Ca^{2+} dependence (both cytosolic and luminal) of all three time constants (Fig. S3). (Details of the Ca^{2+} binding analysis are given in the Supporting Material.)

The model also provides an explanation of how high and low luminal Ca^{2+} differ in the binding of Ca^{2+} during the closed state. Specifically, we find significant overlap between the on and off rates that reproduce the measured time constants, indicating similarities in some Ca^{2+} binding steps. But, we find that the binding of the first Ca^{2+} is stabilized at low luminal Ca^{2+}; the smaller time constants with low luminal Ca^{2+} come from preventing unbinding of the first Ca^{2+}, with the other parameters unchanged (Fig. S3 C).

This very simple Ca^{2+} binding model provides a reasonable explanation of our data, but our analysis is by no means exhaustive; other Ca^{2+} binding models may explain the data. However, because the overarching goal of this study is to show that RyR open times are determined in the closed state, we limit our analysis to providing one possible explanation of what the cytosolic $[Ca^{2+}]$-dependent process is that determines RyR open-time distributions.

The implications of our findings are far-ranging, both for RyR and ion channels in general.

With respect to RyR regulation by cytosolic Ca^{2+}, influencing open time by what occurs during the closed state is probably the simplest way to keep a Ca^{2+}-conducting, Ca^{2+}-sensitive channel from activating itself. If RyR were activated by its own fluxed Ca^{2+}, then some other mechanism would likely be necessary to control the closing of RyRs (e.g., some form of inactivation) lest all the RyRs in a cluster open (via inter-RyR Ca^{2+}-induced Ca^{2+} release) and stay open (via feedthrough activation) until sarcoplasmic reticulum Ca^{2+} is depleted. Moreover, cytosolic Ca^{2+} binding in the closed state is probably the only way for RyR to be sensitive to 1 μM Ca^{2+}. If RyR sensed cytosolic $[Ca^{2+}]$ in the open state, the sensor would have to have extraordinarily fine sensitivity, distinguishing, for example, 50 μM from 51 μM (Fig. S9).

In this picture, Ca^{2+} released during an opening diffuses away and does not appreciably increase the background cytosolic $[Ca^{2+}]$ seen by the RyR in the closed state. If this does not occur (e.g., in the tight geometry of the subsarcolemmal space), then the fluxed Ca^{2+} can reactivate RyR. Although more study is needed, we suspect that this is what occurs when we and other groups found feedthrough activation with Ca^{2+} fluxes ~10 times larger than physiological (1,2). Similarly, with caffeine, with ATP, or without cytosolic Mg^{2+}, the activation site is more sensitive to Ca^{2+} and MOT is increased, and therefore residual Ca^{2+} is more likely to trigger a new opening.

Our analysis also has implications about RyR regulation by luminal Ca^{2+}. It is already known that luminal Ca^{2+} affects RyR gating (11–14), although this is phenomenon is not universal (e.g., the Ca^{2+} sensitivity shift in Fig. 1 A is not present in mouse RyR2 or with the addition of exogenous CSQ (11)) and more studies are necessary. Our study provides evidence that luminal Ca^{2+} can alter function of both the cytosolic activation and inactivation sites. With respect to the inactivation site, low luminal $[Ca^{2+}]$ seems to inhibit inactivation by preventing a drop in open times at high cytosolic $[Ca^{2+}]$ (Figs. S5 and S8). With respect to the activation site, the different time constants for high and low luminal Ca^{2+} in Fig. 3 are direct evidence that the luminal side changes the properties of the cytosolic site. Specifically, the shorter time constants with low luminal $[Ca^{2+}]$ indicate a faster setting of open times compared to high luminal $[Ca^{2+}]$, especially at low cytosolic $[Ca^{2+}]$. Moreover, our modeling suggests that the affinity of the cytosolic Ca^{2+} binding site varies with luminal $[Ca^{2+}]$ (and probably mainly the affinity for the first Ca^{2+}). Possible explanations include the occupancy state of the luminal Ca^{2+} binding site or a change in a luminal regulatory protein (e.g., unbinding) altering the cytosolic activation site architecture (11–14).

Our results also have implications for understanding ion channels in general, not just RyR. For example, our work shows that channel gating is not always a random occurrence. For RyR, we showed that there is memory between the closed and open states through how much Ca^{2+} is bound during the closed state; if the binding process is >30% completed (Fig. S12), then the open-time distributions are the same. At shorter closed times, however, the openings do seem to be more stochastic (Fig. S13).

Overall, our analysis indicates that this memory is vital to physiological RyR2 function so it can sense micromolar cytosolic $[Ca^{2+}]$ and still mediate a large Ca^{2+} flux.

SUPPORTING MATERIAL

Supporting Materials and Methods, 13 figures, and two tables are available at http://www.biophysj.org/biophysj/supplemental/S0006-3495(18)30979-2.

AUTHOR CONTRIBUTIONS

The hypothesis was conceived by D.G. during discussions with M.F. M.F. provided the experimental data and contributed to the analyses and writing. D.G. conceived and performed the analyses and wrote the manuscript.

ACKNOWLEDGMENTS

SUPPORTING CITATIONS

References (15–24) appear in the Supporting Material.

REFERENCES

1. Liu, Y., M. Porta, …, M. Fill. 2010. Flux regulation of cardiac ryanodine receptor channels. *J. Gen. Physiol.* 135:15–27.

2. Xu, L., and G. Meissner. 1998. Regulation of cardiac muscle Ca^{2+} release channel by sarcoplasmic reticulum lumenal Ca^{2+}. *Biophys. J.* 75:2302–2312.

3. Laver, D. R. 2007. Ca^{2+} stores regulate ryanodine receptor Ca^{2+} release channels via luminal and cytosolic Ca^{2+} sites. *Biophys. J.* 92:3541–3555.

4. Laver, D. R., and B. N. Honen. 2008. Luminal Mg^{2+}, a key factor controlling RYR2-mediated Ca^{2+} release: cytoplasmic and luminal regulation modeled in a tetrameric channel. *J. Gen. Physiol.* 132:429–446.

5. Sitsapesan, R., and A. J. Williams. 1994. Gating of the native and purified cardiac SR Ca^{2+}-release channel with monovalent cations as permeant species. *Biophys. J.* 67:1484–1494.

6. Stern, M. D. 1992. Buffering of calcium in the vicinity of a channel pore. *Cell Calcium.* 13:183–192.

7. Zahradníková, A., and I. Zahradník. 1995. Description of modal gating of the cardiac calcium release channel in planar lipid membranes. *Biophys. J.* 69:1780–1788.

8. Zahradníková, A., M. Dura, and S. Györke. 1999. Modal gating transitions in cardiac ryanodine receptors during increases of Ca^{2+} concentration produced by photolysis of caged Ca^{2+}. *Pflugers Arch.* 438:283–288.

9. Saftenku, E., A. J. Williams, and R. Sitsapesan. 2001. Markovian models of low and high activity levels of cardiac ryanodine receptors. *Biophys. J.* 80:2727–2741.

10. Rosales, R. A., M. Fill, and A. L. Escobar. 2004. Calcium regulation of single ryanodine receptor channel gating analyzed using HMM/MCMC statistical methods. *J. Gen. Physiol.* 123:533–553.

11. Chen, H., G. Valle, …, P. Volpe. 2013. Mechanism of calsequestrin regulation of single cardiac ryanodine receptor in normal and pathological conditions. *J. Gen. Physiol.* 142:127–136.

12. Zhang, J., B. Chen, …, S. R. Chen. 2014. The cardiac ryanodine receptor luminal Ca^{2+} sensor governs Ca^{2+} waves, ventricular tachyarrhythmias and cardiac hypertrophy in calsequestrin-null mice. *Biochem. J.* 461:99–106.

13. Qin, J., G. Valle, …, M. Fill. 2008. Luminal Ca^{2+} regulation of single cardiac ryanodine receptors: insights provided by calsequestrin and its mutants. *J. Gen. Physiol.* 131:325–334.

14. Györke, I., N. Hester, …, S. Györke. 2004. The role of calsequestrin, triadin, and junctin in conferring cardiac ryanodine receptor responsiveness to luminal calcium. *Biophys. J.* 86:2121–2128.

15. Sigworth, F. J., and S. M. Sine. 1987. Data transformations for improved display and fitting of single-channel dwell time histograms. *Biophys. J.* 52:1047–1054.

16. Silverman, B. W. 1986. Density Estimation for Statistics and Data Analysis. Chapman & Hall, London, p. 176.

17. Boyce, W. E., and R. C. DiPrima. 1997. Elementary Differential Equations. John Wiley & Sons, New York.

18. Chamberlain, B. K., and S. Fleischer. 1988. Isolation of canine cardiac sarcoplasmic reticulum. *Methods Enzymol.* 157:91–99.

19. Tu, Q., P. Vélez, …, M. Fill. 1994. Streaming potentials reveal a short ryanodine-sensitive selectivity filter in cardiac Ca^{2+} release channel. *Biophys. J.* 67:2280–2285.

20. Beard, N. A., M. G. Casarotto, …, A. F. Dulhunty. 2005. Regulation of ryanodine receptors by calsequestrin: effect of high luminal Ca^{2+} and phosphorylation. *Biophys. J.* 88:3444–3454.

21. Gillespie, D. 2008. Energetics of divalent selectivity in a calcium channel: the ryanodine receptor case study. *Biophys. J.* 94:1169–1184.

22. Gaburjakova, J., and M. Gaburjakova. 2006. Comparison of the effects exerted by luminal Ca^{2+} on the sensitivity of the cardiac ryanodine receptor to caffeine and cytosolic Ca^{2+}. *J. Membr. Biol.* 212:17–28.

23. Szekely, G. J., M. L. Rizzo, and N. K. Bakirov. 2007. Measuring and testing dependence by correlation of distances. *Ann. Stat.* 35:2769–2794.

24. Szekely, G. J., and M. L. Rizzo. 2009. On Brownian distance covariance high dimensional data. *Ann. Appl. Stat.* 3:1266–1269.

Supplemental Information

Ryanodine Receptor Open Times Are Determined in the Closed State

Michael Fill and Dirk Gillespie

ANALYSIS DETAILS

Determining MOT, MCT, and P_o

P_o was determined from the mean open times (MOT) and mean closed times (MCT): $P_o = \left(1 + \text{MCT} / \text{MOT}\right)^{-1}$. For each ionic condition in Fig. 1, P_o was determined for each individual channel separately and then averaged. The error bars are standard errors of the mean.

For both individual channel data (Fig. 1) and pooled channel data (e.g., Fig. 2), MOT and MCT (collectively referred to as MXT) were determined from histograms of the decimal logarithms ($\log_{10}$) of event times (always in ms) with bin size 0.2 as described by Sigworth and Sine (1). In Figs. 2 and S10, the MXT for a given event duration t was determined in the following way. If t was, for example, a closed time duration (as in Figs. 2 and S10A), then all closed/open event pairs (i.e., a closed event and the subsequent opening) with a closed time duration in the interval $\log_{10}(t) \pm 0.1$ were selected. The MOT was then calculated, if this interval contained at least 100 events. For some of the MCT versus open duration curves in Figs. S10B, this threshold was lowered to 10 to include more long open duration events.

Bootstrapping and confidence intervals

Bootstrapping was used to determine confidence intervals of statistical quantities (e.g., the mean of a set of data points). In bootstrapping, for a data set of n values, a new set of data with n values is created by randomly choosing one value from the original data set and then repeating this process of randomly choosing a member of the original data set. Importantly, the values chosen for the new data set are not deleted from the original data set when performing the next random choice. This resampling with replacement allows the same value from the original data set to appear multiple times in the new data set. Having the new data set also contain n values allows statistical measures like standard errors that depend on sample size to be comparable.

Creating a large number N of new, resampled data sets (N in the hundreds or thousands) and calculating their means gives a set of N resampled means that are distributed around the mean of the original data set. The 95% confidence interval around the original mean is given by the 2.5% and 97.5% quantiles of the set of N resampled means. All the confidence intervals shown in the figures were computed using this method for $N = 500$.

We performed two different kinds of bootstrapping: 1) pooling the data from all the channel recordings for one ionic condition and resampling that or 2) resampling entire recordings. In the latter, if there were, for example, 10 different channels recorded for one ionic condition, then we resampled (with replacement) those 10 records and then pooled that data. In this way, we resampled the channel "modes" (Fig. S6) that give the data variability (Figs. S4 and S5). We reasoned that if channels shifted between distinct modes under the same ionic condition (say 3 modes for our example 10 recordings), then with 10 recordings we do not have a sufficient sample size to know what the true ratio of the different modes is (4:3:3 or 5:3:2 and so on). Therefore, resampling the different modes allowed us to better sample all the possibilities.

Both methods always produced the same mean, but different confidence intervals, with method 2 giving larger bounds. These larger confidence intervals overlapped and produced visual clutter in Figs. 2 and S10, so in those figures we show confidence intervals produced with method 1. We fit exponentials to the data in those figures with both sets of confidence intervals, and the resulting time constants were almost identical.

Histogram smoothing

When considering open time distributions for a specific α (Figs. 4 and S12), we first selected all closed events of duration between 0.9α and 1.1α and then computed a histogram of the decimal logarithm of the subsequent open times, as described above. For each α, this was a very small fraction of the total data set and often included only a few hundred events, resulting in very coarse histograms (see Figs. S1 and S2 for examples). These raw histograms are shown in Fig. 4A. To more reliably compute distribution metrics like those in Figs. 4C, 4D, and S12, we used a histogram smoothing technique called kernel density estimation (2).

In this method, the probability distribution function (PDF) $f(x)$ is estimated from independent observations $X_1,...,X_n$ using an approximate PDF:

$$\hat{f}(x) = (nh)^{-1} \sum_{i=1}^{n} K\left(\frac{x-X_i}{h}\right) \tag{1}$$

for a bandwidth h and kernel function K whose integral over the real numbers is 1. Common kernel functions include the Gaussian and our choice, the Epanechikov kernel:

$$K(x) = \begin{cases} \frac{3}{4}(1-x^2) & |x|<1 \\ 0 & \text{otherwise.} \end{cases} \tag{2}$$

The key to the method is to determine an appropriate bandwidth h. We used Silverman's "rule of thumb" that computes h as the minimum of the asymptotic mean integrated square error (2):

$$h = \left(\frac{\|K\|_2^2}{m_2(K)^2 \|G\|_2^2 \, n}\right)^{1/5} \tag{3}$$

where the L_2-norm and the second moment m_2 are

$$\|g\|_2^2 = \int_{-\infty}^{\infty} g(x)^2 \, dx$$
$$m_2(g) = \int_{-\infty}^{\infty} x^2 g(x) \, dx. \tag{4}$$

In Eq. (3), $G(x)$ is the second derivative of $N_{\mu,\sigma}$, the normal distribution with mean μ and standard deviation σ. These parameters are determined by fitting a Gaussian to the histogram of the data points $X_1,...,X_n$.

This method produced very smooth open time distributions that well-reproduced the raw histograms, as shown in Figs. S1 and S2 where the two are compared for various α. The advantage of the smoothed distributions is that they provide a simple function that can be evaluated for any x to easily compute distribution metrics, while at the same time significantly reducing noise due to the roughness of the histograms.
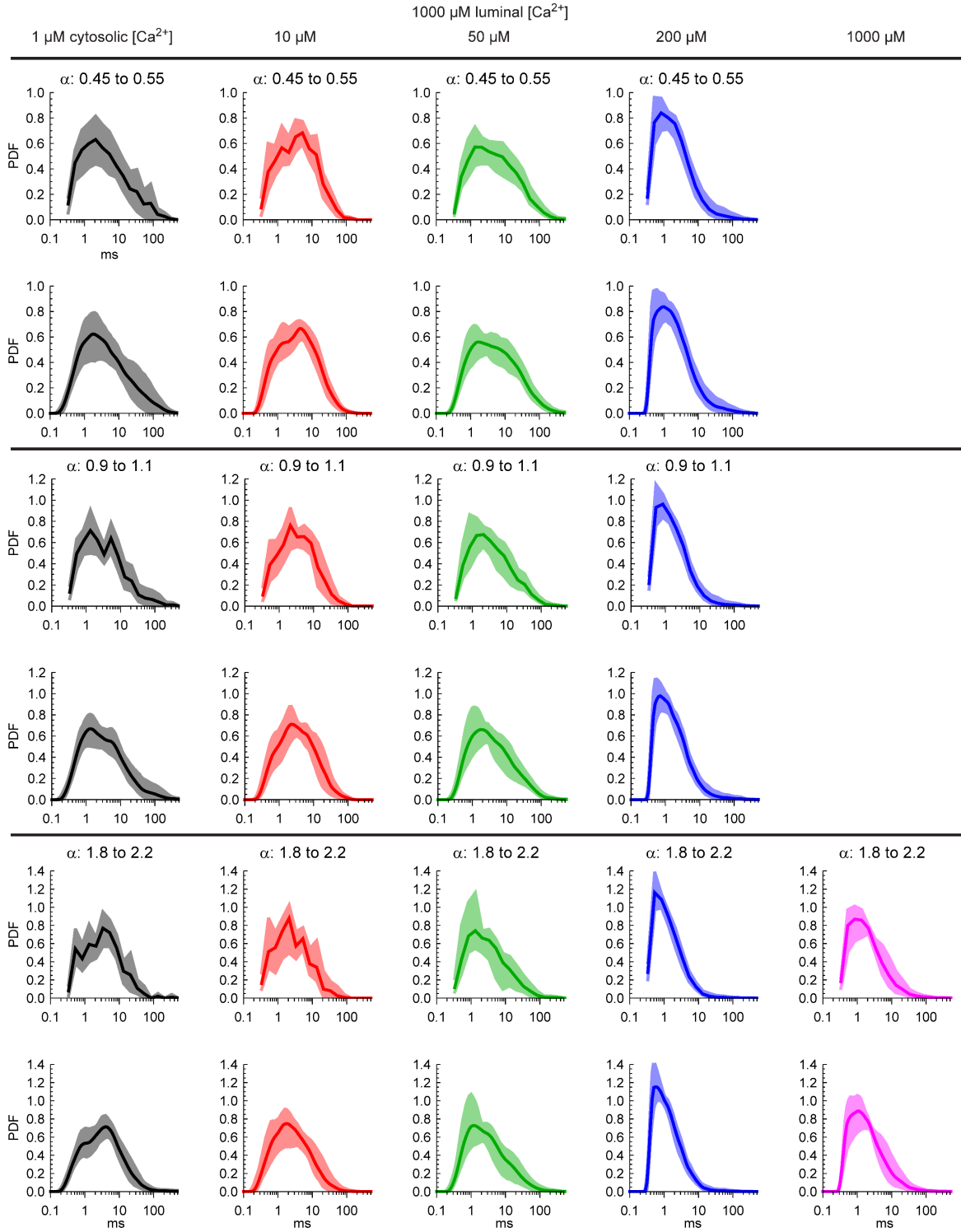
Fig. S1. Probability distribution functions (i.e., histograms with normalized counts in each bin divided by the width of the bin) of open times for high luminal [Ca²⁺], varying cytosolic [Ca²⁺] (columns), and different α. For each α, two lines of graphs are shown: top, the raw data (line) with confidence intervals from bootstrapped channel modes; bottom, the smoothed distributions.
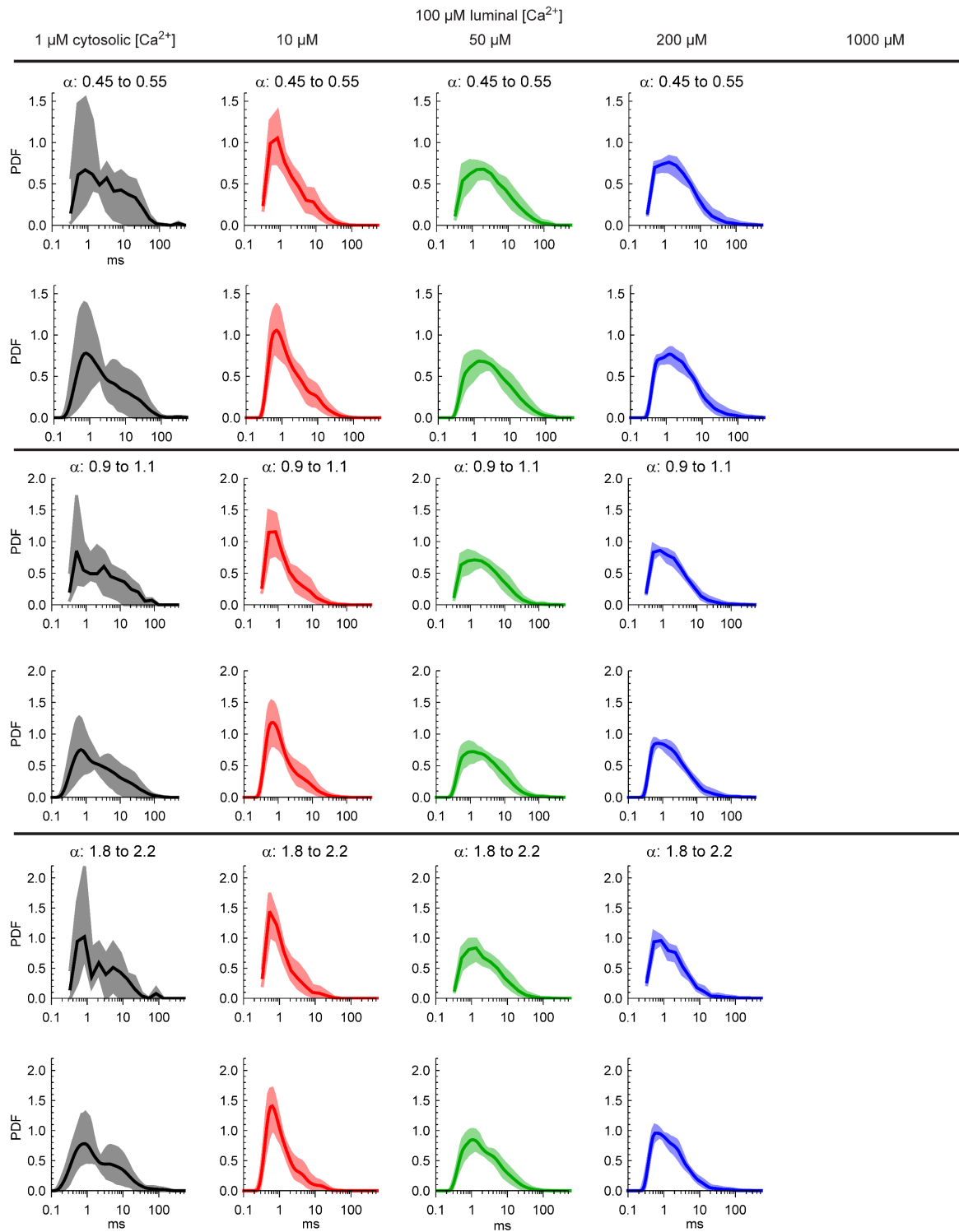
Fig. S2. Same as Fig. S1, but for low luminal [Ca^{2+}].

Fitting time constants

The curves in Fig. 2 where fit to a sum of three exponentials plus a constant. Each data point was weighted according to the reciprocal of the width of the confidence interval shown in the figure (i.e., data with small confidence intervals were weighted more). For the higher cytosolic Ca^{2+} concentrations shown in Fig. S10, a sum of one or two exponentials was fit for 1000 and 200 μM, respectively due to the noise in the data at long event durations. Since long duration events are more rare and the data is more noisy for all cytosolic Ca^{2+} concentrations (see, for example, the green curves in Fig. 2), the fitting procedure sometimes omitted some of the last points, but in the figures all data points are shown. The error bars shown in Figs. 3 and S11 are standard errors of the parameter estimates, and the corresponding 95% confidence intervals are ±1.96 times these errors.

Ca^{2+} binding modeling

We modeled Ca^{2+} binding to the cytosolic side of the RyR by assuming each tetrameric RyR has four Ca^{2+} binding sites, one for each monomer. In our model, each stage of binding one Ca^{2+} has different on and off rates for binding; that is, the binding of, for example, the second Ca^{2+} has different on and off rates from the binding of the third Ca^{2+}. We make no geometric distinction whether Ca^{2+} bound on a monomer is adjacent to one already bound with Ca^{2+} or diagonally opposite such a monomer. The scheme is shown in Figs. S3A and S3B (top). In the former model, four Ca^{2+} can bind to RyR and has four time constants. In the latter model, three can bind and has three time constants and assumes that any three of the four RyR monomers binding Ca^{2+} is sufficient to activate the channel. Both models are consistent with the findings of Sitsapesan and Williams that found at least three is necessary (3).

Specifically, if n is the maximum number of Ca^{2+} that can be bound and p_i is the probability that i have bound, then the equations are:

$$\sum_{i=0}^{n} p_i = 1$$

$$\frac{dp_i}{dt} = ck_{i-1}^{+} p_{i-1} - k_i^{-} p_i - ck_i^{+} p_i + k_{i+1}^{-} p_{i+1} \quad (1 \le i \le n-1) \tag{5}$$

$$\frac{dp_n}{dt} = ck_{n-1}^{+} p_{n-1} - k_n^{-} p_n$$

where c is the cytosolic Ca^{2+} concentration. This is a system of inhomogeneous, linear, first-order ordinary differential equations that can be made homogeneous by subtracting off the steady-state solution. This homogeneous system is analytically solvable (4). In particular, the solution is a sum of n decaying exponentials with the time constants being the negative reciprocals of the eigenvalues of a matrix derived from Eq. (5).

We determined the on and off rates for each step by randomly selecting parameters and checking whether they matched our measured time constants, specifically whether they were within the error bars or confidence intervals (twice the error bars) of the time constants in Fig. 3. (In the case of $n = 4$ we used the three largest time constants.) Error bars were used for high luminal Ca^{2+} and confidence intervals for low luminal Ca^{2+} because error bars were smaller in the latter case. We selected those parameter sets that matched 11 or 12 of our 12 time constants.

The distributions of these on and off rates is shown in Figs. S3A and S3B (bottom). Because there are 8 parameters for the $n = 4$ model (Fig. S3A) and 12 data points, the parameters of this model are poorly determined, ranging over several orders of magnitude. In contrast, the 6

5

parameters of the $n = 3$ model (Fig. S3B) are well defined, with the exception of k_1^-; the three time constant versus [Ca^{2+}] curves were independent of k_1^- for $k_1^- < \sim 10$. Because the parameters were better defined, we focused on this model.

In Fig. S3B we found substantial overlap between some of the on and off rates for high and low luminal Ca^{2+} (purple regions); k_1^+, k_2^+, and k_2^- are very similar while k_0^+, k_1^-, and k_3^- are distinctly different. Because two of the three distinct parameters are involved in the binding of the first Ca^{2+}, we hypothesized that low luminal Ca^{2+} stabilizes this first binding by substantially reducing the off rate (k_1^-) and that perhaps this is enough to explain the differences in the high and low luminal Ca^{2+} time constants (ignoring k_3^- for now). This, indeed, seems to be the case.

In Fig. S3C we show the three time constants for high (top row) and low (bottom row) luminal Ca^{2+} by using the subset of the high luminal Ca^{2+} parameters that have the same k_1^+, k_2^+, and k_2^- as the low luminal Ca^{2+} case and then changing k_0^+ and k_1^- to the low luminal Ca^{2+} range. In this way, we test whether we can reproduce the low luminal Ca^{2+} time constants by changing only the on and off rate of the first Ca^{2+} binding step. Specifically, we picked the on and off rates in the following way: first, from the set of on and off rate parameters for high luminal Ca^{2+}, we chose those that overlapped with the low luminal parameters for k_1^+, k_2^+, and k_2^- (purple regions in Fig. S3B); second, for each of these 570 different parameter sets, we changed the k_0^+ to a randomly chosen value between 10 and 100 µM^{-1}s^{-1} (the low luminal range for this parameter) and k_1^- to a value between 0.01 and 10 s^{-1} (the low luminal range for this parameter); third, we did not change k_3^-. Fig. S3C (bottom row) shows that all three low luminal Ca^{2+} time constants are well-reproduced by only stabilizing the binding of the first Ca^{2+}. As for k_3^-, stabilizing the binding of the third Ca^{2+} by reducing its off rate (from the high luminal Ca^{2+} value) only changed the low luminal Ca^{2+} time constants for 1 µM cytosolic [Ca^{2+}] (data not shown); that is, holding on to the third bound Ca^{2+} only has an impact at very low cytosolic [Ca^{2+}], compared to the large-scale impact of stabilizing the first bound Ca^{2+}.

Therefore, we conclude that—from the point of view of this simple model—the main effect of low luminal Ca^{2+} (vis a vis cytosolic Ca^{2+} binding) is to facilitate Ca^{2+} binding in the closed state by making it difficult for the first cytosolic Ca^{2+} that binds to unbind. (The other effect of low luminal Ca^{2+} is to shift the open time distributions to shorter openings (Fig. 4C, compare bottom row).) However, this model is very simplified, and we have not studied other possible models. Our analysis does show that this explanation is plausible for reasonable binding on and off rates. This level of analysis supports our proposal that RyR open times are determined in the closed state; our goal is not determine the exact nature of the cytosolic Ca^{2+}-dependent process, but rather to begin providing data-driven and reasonable explanations of what this process could be.
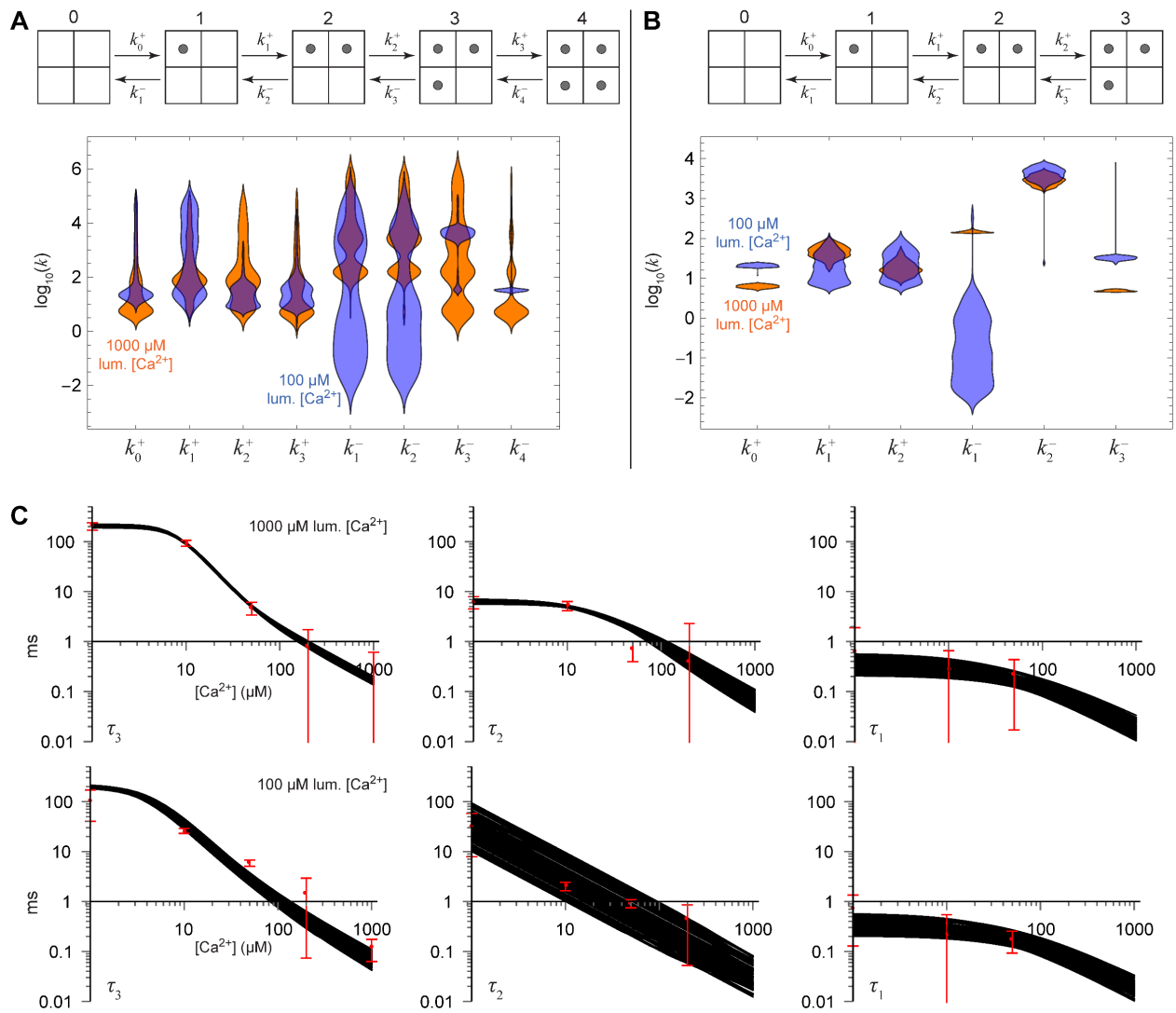
Fig. S3. Models of cytosolic Ca^{2+} binding. (A) Scheme (top) with up to 4 Ca^{2+} binding to the RyR with associated on/off rate constants (bottom) that went through at least 11 of the 12 the confidence intervals (twice the error bars) in Fig. 3 for both high (orange) and low (blue) luminal Ca^{2+}. (B) Same as panel A except the model only considers binding up to 3 Ca^{2+}. (C) The three time constants of the model in panel B as a function of cytosolic [Ca^{2+}], calculated as described in this section.

EXPERIMENTAL DETAILS

Single-RyR recordings

Studies were undertaken with approval by the Animal Care and Use Committee of Rush University Medical Center.

Sarcoplasmic reticulum (SR) microsomes were generated from rat ventricular muscle. Microsomes were isolated as previously described (5) and stored at –80 C. Lipid bilayers (diameter 100 µm) were comprised of a 5:4:1 mixture (50 mg/ml in decane) of phosphatidylethanolamine, phosphatidylserine, and phosphatidylcholine. Solution on one side of the bilayer (cis) was virtually grounded. The cis solution initially contained a HEPES-Tris solution (250 mM HEPES and 120 mM Tris, pH 7.4). The solution on the other side of the bilayer was initially a HEPES-Ca^{2+} solution (50 mM HEPES and 10 mM $Ca(OH)_2$, pH 7.4). The SR microsomes (5–15 µg) were added to the cis solution along with 500 mM CsCl and 2 mM $CaCl_2$ to promote microsome fusion. Fusion of RyR2-containing microsome results in the RyR2's cytosolic side facing the cis compartment and its luminal domains in the other compartment (6).

After single-RyR2 activity was observed, the cytosolic solution was immediately replaced to establish the various test recording conditions. The luminal solution was changed 10 minutes later. Specifically, the cytosolic recording solution contained 1–1000 µM of free Ca^{2+}, 0.5 mM EGTA, 1 mM of free Mg^{2+}, 5 mM of total ATP, 114 mM Tris, and 250 mM HEPES (pH 7.4). (All solutions were designed using the MAXC program at maxchelator.stanford.edu). The luminal recording solution contained 100 or 1000 µM free Ca^{2+} and 200 mM Cs^+-HEPES (pH 7.4). Final recording solutions are listed in Table S1.

The 10 minute interval before changing the luminal solution means the RyR2 was exposed to 10 mM Ca^{2+}, sufficiently long to promote calsequestrin (CASQ) dissociation (if any CASQ was associated with the RyR2). This CASQ stripping process is analogous to that applied by others (7-9). CSQ was stripped from the RyRs so that the RyR2 tested were not subject to CASQ-based luminal regulation and so that a homogenous population of RyRs was studied, as not all channels in this preparation are associated with CSQ (7).

All recordings were done at room temperature with current sampled at 50 µs/point (20 kHz) and filtered at 1 kHz. No correction for missing events was made. Representative current traces may be found in Ref. (10) where some of the data was previously published The applied potential was 20, 30, or 40 mV to produce luminal-to-cytosolic cation flux. Individual recordings were performed with one applied potential, and most ionic conditions had recordings with at least two voltages. The 10 µM cytosolic [Ca^{2+}] with high luminal Ca^{2+} (Fig. 1B) was the only condition that also included 10 mV driving potential. The potential did not affect P_o, as shown in Fig. 1B for a representative example.

	Cs+	Tris+	Ca2+ (free)	Mg2+ (free)	ATP (total)
cytosolic	0	114 mM	1–1000 µM	1 mM	5 mM
luminal	200 mM	0	100, 1000 µM	0	0

Table S1. Details of the recording solutions.

Single-channel analysis was done using pCLAMP9 software (Molecular Devices). The deadtime of the filter was ~0.185 ms. When we paired closures and the next opening (or opening and next closure), we discarded all event pairs where either duration was <0.375 ms (twice the deadtime); that is, we take 0.375 ms as the shortest reliably-measurable event time and only analyzed events of duration as long or longer than that. Table S2 shows details of the recordings.

cyto [Ca^{2+}] (µM)	lum [Ca^{2+}] (µM)	# of channels	total recorded open time (min)	total recorded closed time (min)	# of openings
1	1000	16	4.201	55.946	26,749
10	1000	13	35.689	40.965	165,662
50	1000	13	42.773	11.403	129,124
200	1000	14	18.437	8.157	331,197
1000	1000	8	10.661	3.025	160,985
1	100	9	2.340	29.887	25,769
10	100	12	14.962	31.264	190,290
50	100	20	47.892	20.621	294,667
200	100	14	18.404	5.766	205,454
1000	100	9	15.980	1.005	51,784

Table S2. Details of the single-channel recordings: cytosolic [Ca^{2+}] (column 1), luminal [Ca^{2+}] (column 2), number of channels (column 3), total number of minutes in the open and closed states across all recordings (columns 4 and 5). Column 6 lists the total number of openings across all recordings, which is equal to the number of closings ±1.

Ca^{2+} current calculations

The Ca^{2+} currents in Figs. 1B and S9 were computed using the model of Gillespie (11). In this model, individual ionic currents are computed from the physics of cations competing for the selectivity that is crowded with the four aspartates (D4899 in the RyR1 numbering scheme) that define the selectivity filter. In the Ref. (11) and subsequent papers, the model was verified by reproducing existing single-RyR data and predicting new phenomena (e.g., anomalous mole fraction effects) that were later confirmed with experiments.

Channel variability

Even with many individual channels (n=8–20) and long recordings, we found large variability between channels. Specifically, channel P_o vary greatly between channels under the same ionic conditions (Fig. S4) because both MCT and MOT vary greatly (Fig. S5). This is independent of the length of the recordings, as can be seen in Figs. S4 and S5 where the length of the recordings is shown next to many of the data points (space permitting). This is also independent of applied voltage (not shown). Therefore, we conclude that, in our experimental preparation at least, this variability is natural and inherent to RyR.

Interestingly, however, the variability is not due to individual channels behaving randomly differently. We found that channel open and closed time distributions cluster into groups; that is, the channels exhibit a small number of distinct modes of gating under the same ionic conditions. This is shown in Fig. S6 for the 13 channels with 50 µM cytosolic [Ca^{2+}] and 1000 µM luminal [Ca^{2+}]. While there is a wide distribution of MCTs and MOTs (Fig. S5, left column, green points), the open and closed time distributions of channels #3, 5, 6, and 10 are very similar in shape (two rounded peaks with closed-time peak to the left of the open-time peak) while the other channels' distributions are similar to each other (tall, sharply peaked closed times and broad, long-time skewed open times), but not to the 3-5-6-10 group.

This kind of clustering is summarized in Fig. S6B. When MOT is plotted against MCT, the different modes become clear. In this particular example, there are two modes (maybe three depending on how one categorizes channel #8), one with short openings and longer closings and one with long openings and shorter closings. We find this clustering phenomenon with all the ionic conditions we recorded; each time channels grouped into 2–4 clusters like in Fig. S6B.

It should be noted that none of our analysis actually assigns modes to a channel. As can be seen with channel #8 in Fig. S6B, this is a subjective process. Moreover, in a few recordings we observed channels switching modes (not shown). Instead, our analysis embraces the knowledge that channels exhibit different modes by doing a bootstrap resampling of entire recordings (and therefore of the different modes), but we never explicitly group channels together into modes.

Lastly, Fig. S6B also shows that much of the large range of MXTs seen in Figs. S5 comes from outliers in the individual recordings. In Fig. S6B we only used opening and closing times in the 95th percentile and below, which significantly reduces the spread of the MXTs (and also shows the clustering more clearly). This indicates that even for recordings lasting up to 8 minutes, extremely long openings and closing can still skew the data. This is why pooling the data, as we do, obtained from many channels is important. Then, the recordings with long events are mixed with recordings that do not have these rare events, building a large data set of openings and closings that are more statistically representative of the channel's overall behavior.

Our analysis is based on pooled data and not on data from individual modes because grouping recordings into modes is subjective and arbitrary. Moreover, there is insufficient data in each mode group to perform the analysis. This is because the analysis relies on many small subsets of the data and each of these must be large enough to be statistically reliable. Specifically, each mode group of channels generally consists of 1 to ~5 recordings, and these do not have sufficient number of the long closings that are vital to the analysis; even in the pooled data there is significant noise at long closed time durations (Figs. 2 and S9A). Moreover, there are an insufficient number of opening events to make reasonably smooth histograms of open times; for specific α, in particular, the histograms have too few counts to be statistically reliable unless pooled data is used.
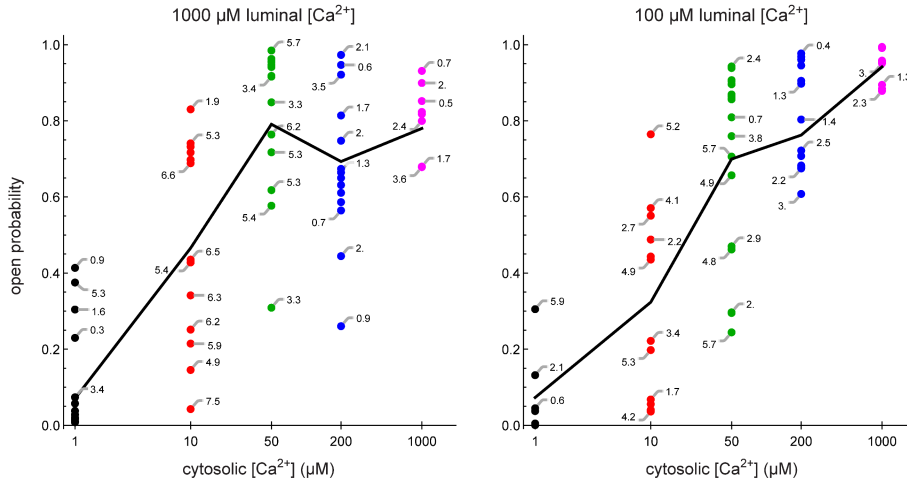
Fig. S4. Variability in the open probability of each individual channel recording. Each point is the P_o of one recording and the line is a linear connection of the mean of the pooled data meant to guide the eye. The numbers next to some of the points are the length of the recording in minutes.
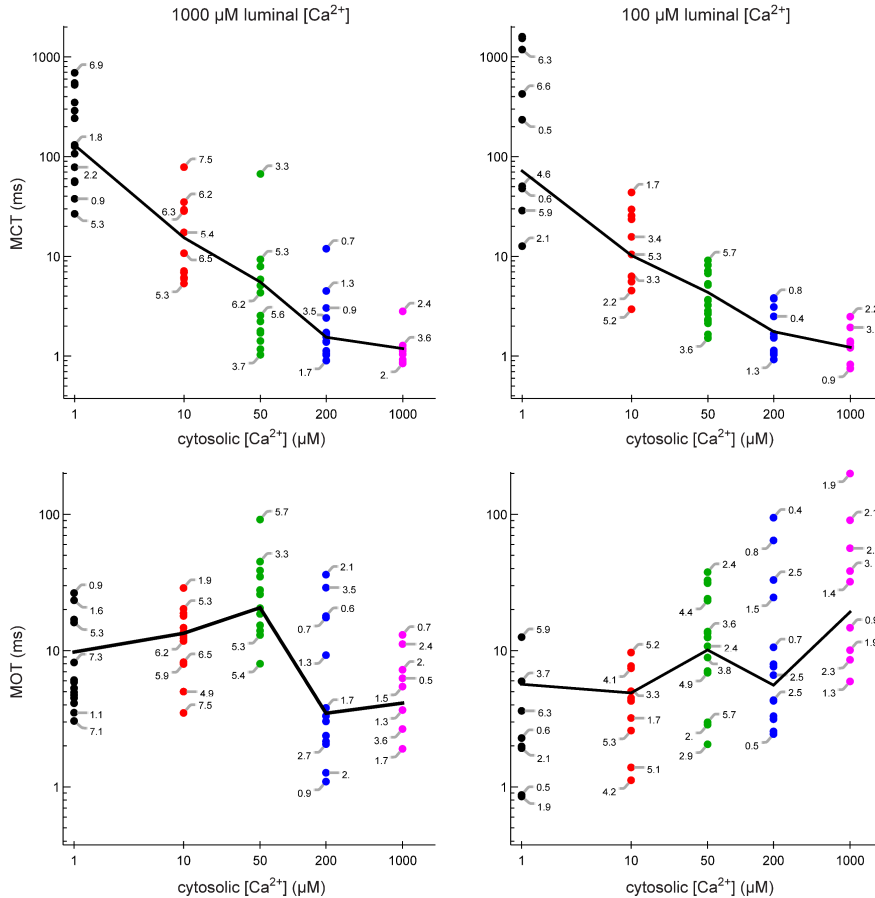

Fig. S5. Variability in MCT (top) and MOT (bottom) of each individual channel recording, with each point one recording. Note the log scale on the *y*-axis. The numbers next to some of the points are the length of the recording in minutes. The line is a linear connection of the mean of the pooled data and is meant to guide the eye.

11
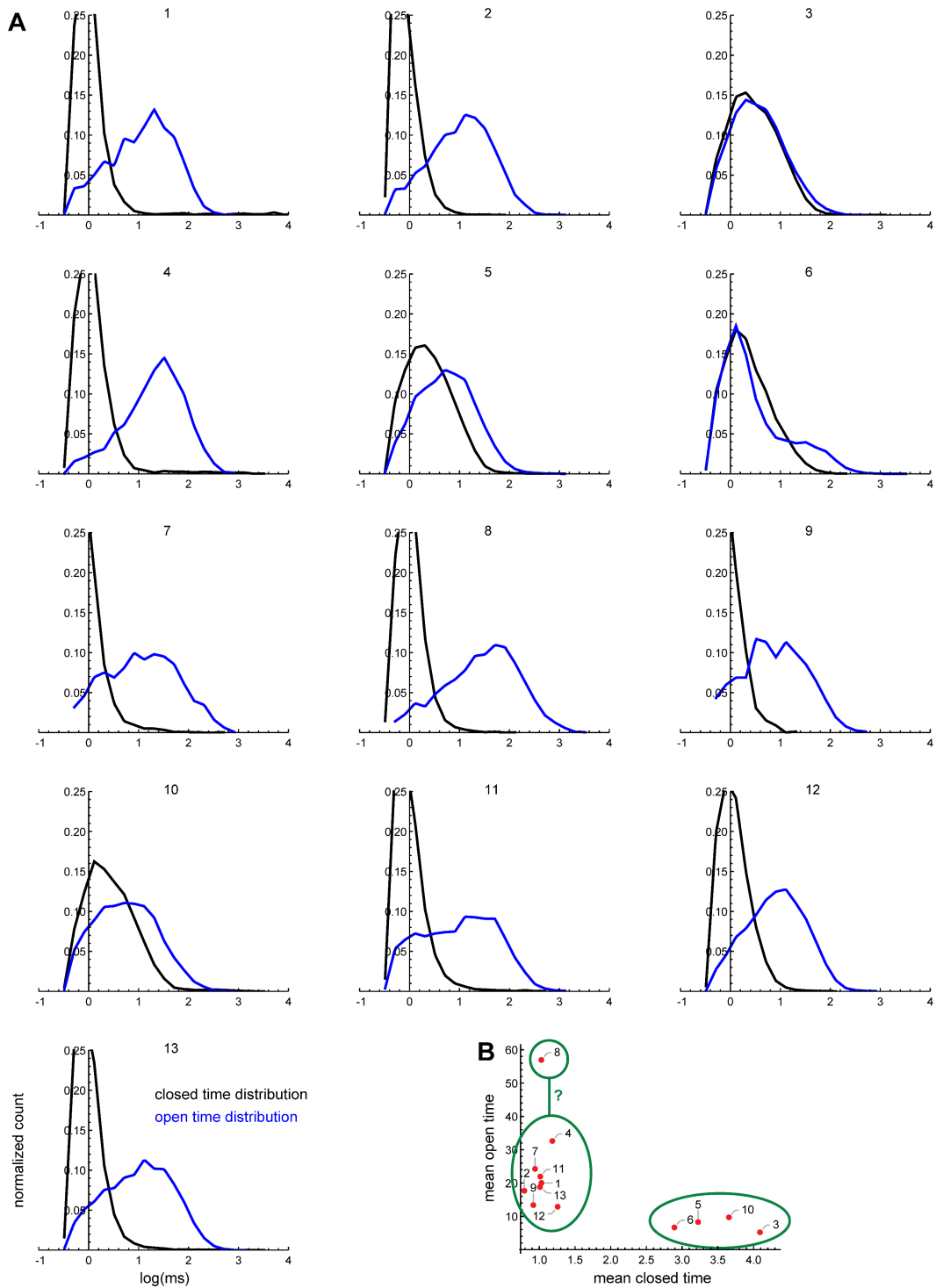
Fig. S6. (A) The closed (black) and open (blue) time distributions (normalized count in each bin) for each of the 13 different channels (reference number at the top for each plot) we measured with 50 μM cytosolic $[Ca^{2+}]$ and high luminal Ca^{2+}. (B) MOT versus MCT for these channels, with the channel reference number shown near each point. These values differ slightly from those in Fig. S5 because here extremely long openings and closings were not included (only up to the 95th percentile). This shows the groupings into different modes (green ovals) more clearly.

Inactivation

When examining MXTs in Fig. S5, one sees several trends. First, MCT always steadily decreases as cytosolic [Ca^{2+}] increases (Fig. S5, top row). This is not just in the average of all the pooled recordings, but also in the extremes of the individual recordings, i.e. the envelope around the mean from the variability across channels. Second, for low luminal Ca^{2+}, MOT increases as cytosolic [Ca^{2+}] increases. While the mean may not be monotonic, the envelope shows that trend. Lastly, for high luminal Ca^{2+}, MOT decreases sharply between 50 µM and 200 µM (Fig. S5, bottom left). This is also seen in the envelope around the mean, indicating that all channel modes experience this drop. We interpret this as an indication that inactivation is occurring at 200 µM and higher cytosolic [Ca^{2+}] and high luminal Ca^{2+}, but not at low luminal Ca^{2+}. (The statistical significance of this drop in MOT is discussed below.) This is consistent with RyR's known cytosolic inactivation site with millimolar Ca^{2+} sensitivity.

Surprisingly, our fitting of the P_o versus cytosolic [Ca^{2+}] in Fig. 1 did not reveal evidence of inactivation, although a term for it was included in the fitting:

$$P_o(c) = \frac{B}{1 + K_{act}/c} - \frac{B}{1 + K_{inact}/c} \tag{6}$$

where B is the maximum P_o and K_{act} and K_{inact} are the dissociation constants of the activation and inactivation sites, respectively. In the fit shown in Fig. 1, K_{inact} was several thousand micromolar, indicating no inactivation for the concentrations we used.

To analyze this further and try to understand the contradictory conclusion from the fitting and the drop in MOT, we re-analyzed the fitting by bootstrapping different recordings at each cytosolic [Ca^{2+}]. That is, if there were n recordings for a cytosolic [Ca^{2+}], we randomly selected n different recordings (with replacement), pooled that data, computed the P_o, and fit that P_o versus cytosolic [Ca^{2+}] curve. We did this 1000 times. A sample of 100 fitted curves is shown in Fig. S7. We found that 1/3 of the time the fit revealed inactivation with high luminal Ca^{2+}, but only 1/50 with low luminal Ca^{2+}. This indicates that inactivation might be present at high luminal Ca^{2+} but not at low. Overall, this analysis suggests that curve-fitting of P_o is not definitive for inactivation: not finding inactivation in the fitting does not indicate a lack of inactivation.
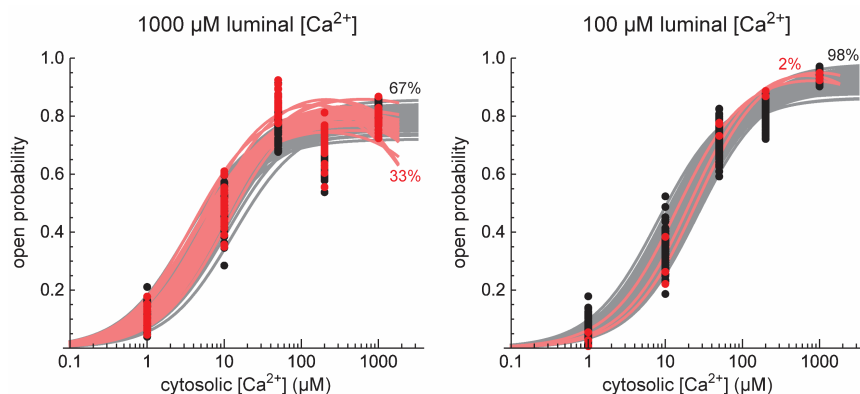

Fig. S7. Bootstrap resampling of MXTs and recalculation of P_o. The light red curves are those where there was a maximum in the curve, the gray curves there was not. The black (red) data points are the resampled P_o used in the fit for the gray (light red) curves. The % indicated are the percent of curves from 1000 fits.

Next, we examine the statistically significance of the drop in MOT at high luminal Ca^{2+}. Since the underlying open time distributions are not identically distributed (Fig. S6), standard tests of significance are not applicable. Instead, we use bootstrapping of the different channel modes to sample all possible MOTs for 50, 200, and 1000 µM cytosolic Ca^{2+}. By sampling many different ratios of channel modes for each cytosolic $[Ca^{2+}]$, we can compute the distribution of all possible MOTs at each concentration. Fig. S8 shows these probability distribution functions of the MOTs for 50 (red line), 200 (blue line), and 1000 µM (magenta line) cytosolic Ca^{2+}. In this figure, the probability of having an MOT between t and $t + \Delta t$ can be found by integrating the curve between those times.

The figure shows that the MOT distributions for 50 µM and 200 µM do not overlap. In other words, the probability is virtually 0 that the "true" MOTs for 50 µM and 200 µM are similar. Therefore, the drop in MOT between 50 and 200 µM cytosolic Ca^{2+} is statistically significant. In addition, Fig. S8 shows that the variability in the channel data makes it impossible to determine whether the decrease in MOT continues between 200 and 1000 µM cytosolic Ca^{2+}; the PDFs are too similar to know whether the true MOT at 200 µM is greater than the MOT at 1000 µM.

Lastly, we note that Gaburjakova and Gaburjakova (12) also found a sharp drop in MOT in caffeine-exposed RyRs at ~200 nM cytosolic $[Ca^{2+}]$. However, there was also a drop in MCT and P_o did not change. This is not behavior one would attribute to inactivation and is qualitatively different than our findings. In our experiments, there is no a concomitant drop in MCT; MCT decreases continuously (Fig. S5). This is consistent with inactivation, especially since it occurs at the higher cytosolic $[Ca^{2+}]$ where one usually sees inactivation.
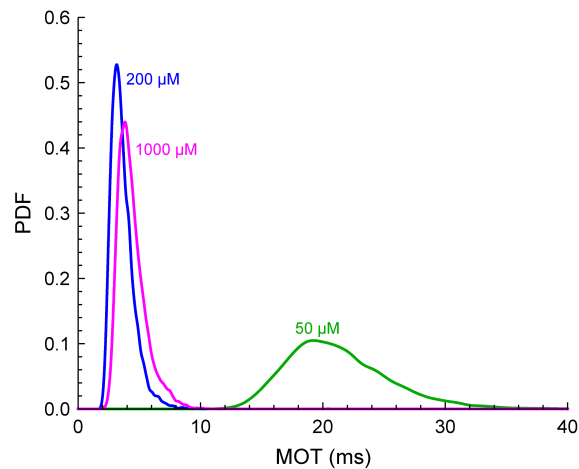

Fig. S8. The probability distribution functions (PDFs) of possible MOTs for 50 (red line), 200 (blue line), and 1000 µM (magenta line) cytosolic Ca^{2+} with 1000 µM luminal Ca^{2+}. Each line is the distribution of 10,000 MOTs calculated by bootstrap resampling the recordings at one cytosolic $[Ca^{2+}]$, pooling the data, and computing the MOT.
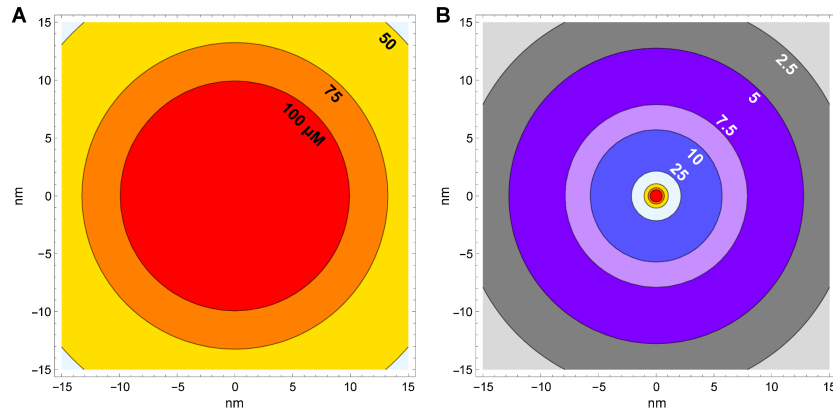
ADDITIONAL FIGURES

Ca²⁺ around an open RyR

Fig. S9. We solved the steady-state reaction-diffusion equations for 1 µM Ca^{2+} and 0.5 mM EGTA (as used in the experiments) in a spherically symmetric geometry. We used a bulk diffusion coefficient for Ca^{2+} ($0.79 \cdot 10^{-9}$ m^2/s) and the same diffusion coefficient for EGTA. The on and off rates for Ca^{2+} binding were 2 µM^{-1}s^{-1} and 2 s^{-1}, respectively. The results are shown in the figure. (A) A contour plot of Ca^{2+} concentration on the face of a 30×30 nm RyR for the largest Ca^{2+} current used in the experiments of 0.95 pA as calculated by the model of Gillespie (11), for a luminal Ca^{2+} concentration of 1000 µM and 40 mV applied voltage. The concentrations of the other permeating cations were as in the experiments (cytosolic: 1 mM Mg^{2+}, 0 mM Cs$^+$, 0.1 µM Ca^{2+}; luminal: 0 mM Mg^{2+}, 200 mM Cs$^+$). Contours are labeled with the concentration in µM. The yellow region has concentration between 50 and 75 µM. (B) Ca^{2+} concentration contours for the lowest Ca^{2+} current used in the experiments, 0.050 pA, for a luminal Ca^{2+} concentration of 100 µM and 10 mV applied voltage (other ion concentrations as above). The red, orange, and yellow colors represent the same concentrations as in panel A.

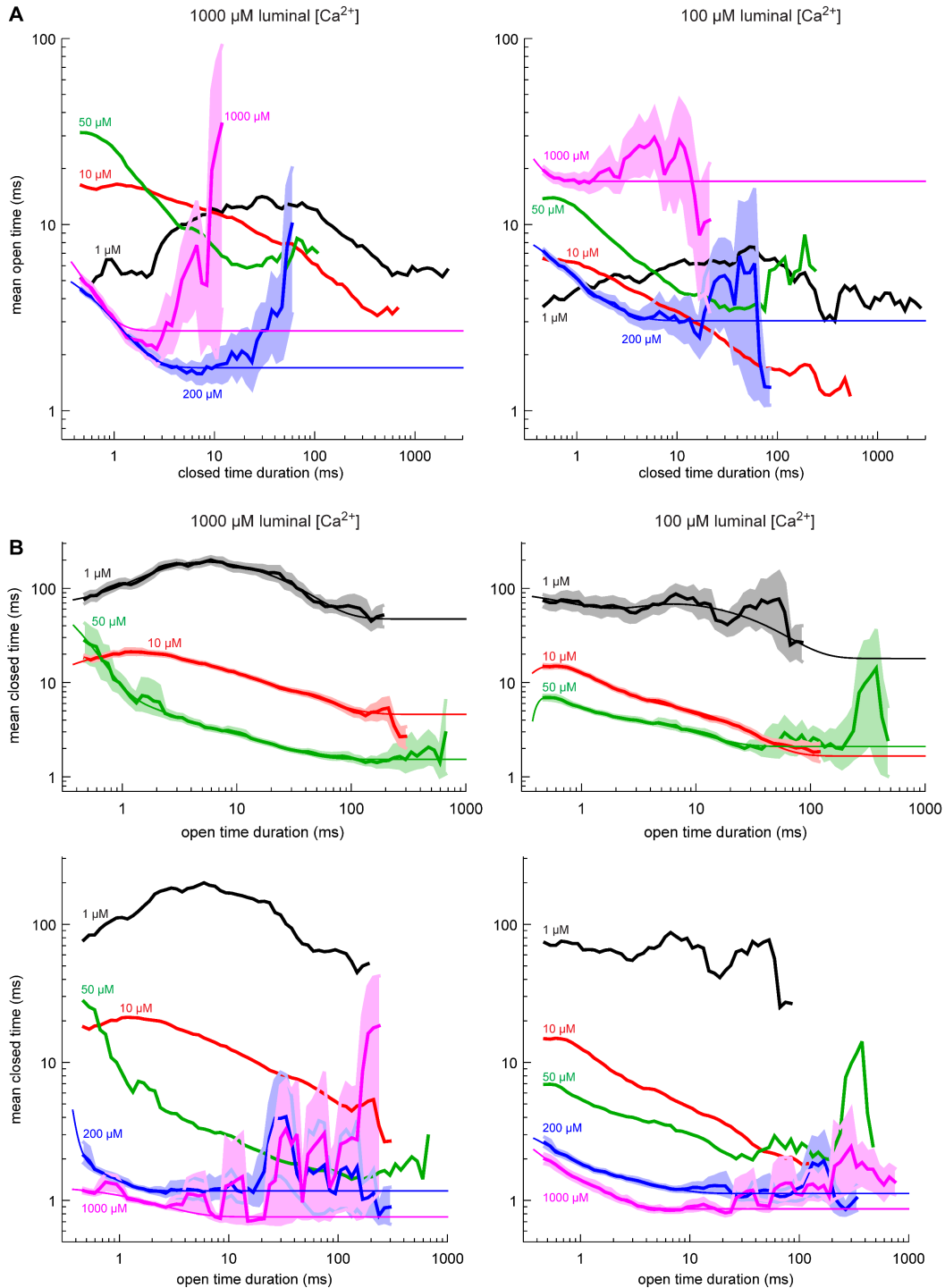# *Mean open (closed) time versus closed (open) time duration*

Fig. S10. (A) Same as Fig. 2 in the main text, except that high cytosolic [Ca^{2+}] are shown for MOT versus closed time duration. The solid lines from Fig. 2 are included for reference. (B) MCT versus open time duration.
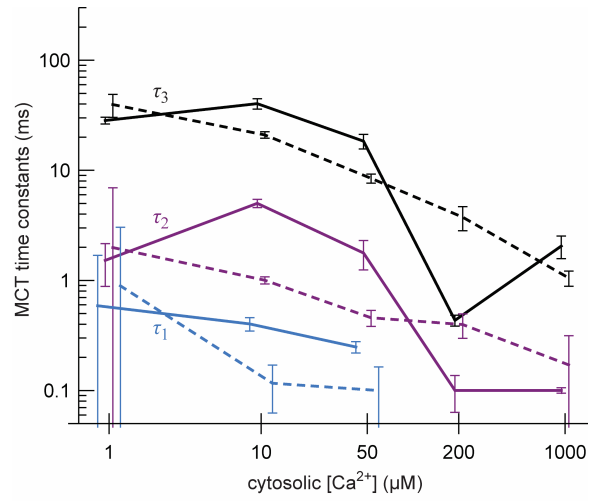
Fig. S11. Same as Fig. 3, except that the time constants are for Figs. S10B.

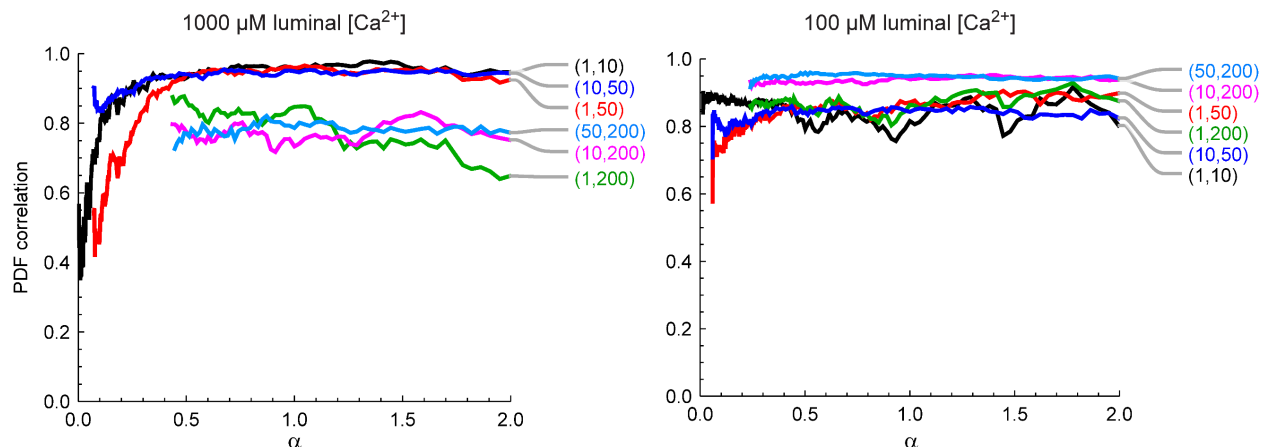### *Speed of convergence to same open time distributions*

Fig. S12. How far through the cytosolic Ca^{2+} binding process until the open time distributions are the same? The *y*-axis shows the Pearson correlation coefficient of the smoothed open time probability distributions for all pairs of cytosolic $[Ca^{2+}]$ (number pairs in parentheses in µM). Specifically, for each α and each pair of cytosolic $[Ca^{2+}]$ (c_1,c_2), a smoothed histogram of open time probabilities (Figs. S1 and S2) for c_1 and a histogram for c_2 were created, plotted parametrically against each other, and the Pearson correlation computed; if the distributions are the same, then the parametric plot is a straight line of slope 1. A correlation coefficient of $+1$ means that they form a line, but not necessarily one of slope 1. However, combined with the analysis in Fig. 4 that shows high similarity between the distributions, a correlation of $+1$ means the slope of the parametric plot must be close to 1, which was confirmed with direct fits of the slopes (not shown).

The curves are the average of 500 bootstrapped channel modes at each α. For both high and low luminal $[Ca^{2+}]$, the red line (1 µM versus 50 µM) took the longest to complete, by $\alpha \approx 0.3$. For high luminal $[Ca^{2+}]$ (left panel), the curves with 200 µM (green, magenta, and light blue) should *not* correlate since the 200 µM distributions at all α are different from the 1, 10, and 50 µM distributions (Fig. 4B); these correlations continue to decrease for $\alpha > 2$ (not shown).

Openings after short closings are more stochastic
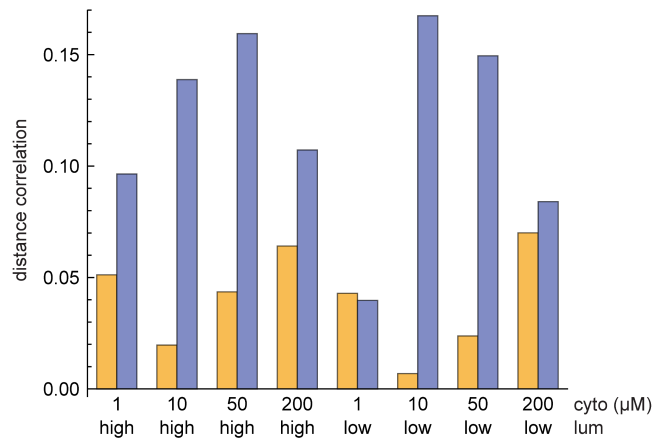

Fig. S13. Correlation between closed times and next open times for closed time durations <1 ms (orange bars) and >1 ms (blue bars) for the cytosolic and luminal conditions listed below each pair. After a short closure (orange bars), there is less correlation between the closed time and next open time, indicating more randomness in the opening time durations than after a long closure (blue bars); that is, the openings after short closures are more stochastic than after long closures.

The correlation metric is the distance correlation (13,14) which has several properties different from the more standard Pearson correlation coefficient: 1) distance correlation measures nonlinear correlations (with values between 0 and 1) whereas the Pearson correlation is sensitive to a linear relationship between two variables (with values between –1 and 1); 2) a Pearson correlation of 0 only indicates that the variables are not linearly correlated, not that they are independent, while distance correlation is 0 if and only if the variables are independent; and 3) a relatively low distance correlation of 0.1 still indicates a fair amount of nonlinear correlation (distance correlation is 1 only if the variables are perfectly linearly correlated).

REFERENCES

1. Sigworth, F. J. and S. M. Sine. 1987. Data transformations for improved display and fitting of single-channel dwell time histograms. *Biophys. J.* 52:1047-1054.
2. Silverman, B. W. 1986. Density Estimation for Statistics and Data Analysis. London: Chapman & Hall. 176 p.
3. Sitsapesan, R. and A. J. Williams. 1994. Gating of the native and purified cardiac SR Ca^{2+}-release channel with monovalent cations as permeant species. *Biophys. J.* 67:1484-1494.
4. Boyce, W. E. and R. C. DiPrima. 1997. Elementary Differential Equations. New York: John Wiley & Sons.
5. Chamberlain, B. K. and S. Fleischer. 1988. Isolation of canine cardiac sarcoplasmic reticulum. *Methods Enzymol.* 157:91-99.
6. Tu, Q., P. Velez, M. Brodwick, and M. Fill. 1994. Streaming potentials reveal a short ryanodine-sensitive selectivity filter in cardiac Ca^{2+} release channel. *Biophys. J.* 67:2280-2285.
7. Qin, J., G. Valle, A. Nani, A. Nori, N. Rizzi, S. G. Priori, P. Volpe, and M. Fill. 2008. Luminal Ca^{2+} regulation of single cardiac ryanodine receptors: Insights provided by calsequestrin and its mutants. *J. Gen. Physiol.* 131:325-334.
8. Györke, I., N. Hester, L. R. Jones, and S. Györke. 2004. The role of calsequestrin, triadin, and junctin in conferring cardiac ryanodine receptor responsiveness to luminal calcium. *Biophys. J.* 86:2121-2128.
9. Beard, N. A., M. G. Casarotto, L. Wei, M. Varsányi, D. R. Laver, and A. F. Dulhunty. 2005. Regulation of ryanodine receptors by calsequestrin: Effect of high luminal Ca^{2+} and phosphorylation. *Biophys. J.* 88:3444-3454.
10. Chen, H., G. Valle, S. Furlan, A. Nani, S. Gyorke, M. Fill, and P. Volpe. 2013. Mechanism of calsequestrin regulation of single cardiac ryanodine receptor in normal and pathological conditions. *J. Gen. Physiol.* 142:127-136.
11. Gillespie, D. 2008. Energetics of divalent selectivity in a calcium channel: The ryanodine receptor case study. *Biophys. J.* 94:1169-1184.
12. Gaburjakova, J. and M. Gaburjakova. 2006. Comparison of the effects exerted by luminal Ca^{2+} on the sensitivity of the cardiac ryanodine receptor to caffeine and cytosolic Ca^{2+}. *J. Membr. Biol.* 212:17-28.
13. Szekely, G. J., M. L. Rizzo, and N. K. Bakirov. 2007. Measuring and testing dependence by correlation of distances. *Ann. Statist.* 35:2769-2794.
14. Szekely, G. J. and M. L. Rizzo. 2009. Brownian distance covariance. *Ann. Appl. Stat.* 3:1236-1265.